AIAA JOURNAL
Vol. 30, No. 3, March 1992

Computing Boundary Forces Due to Unsteady, Inviscid, Incompressible Flow

S. R. Breit,* W. C. Coney,† A. L. Dickinson,‡ and J. R. Webb§
Bolt, Beranek and Newman, Inc., Cambridge, Massachusetts 02138

Recently, several investigators have implemented time-accurate finite difference simulations of incompressible flows based on the method of artificial compressibility. Here we validate the method against the discrete vortex method on the problem of a compact vortex being convected by an inviscid mean flow through a converging/diverging channel. This can be regarded as a model problem that isolates the effect of finite airfoil thickness on the interaction of a cascade with a nonuniform inflow. Good qualitative agreement between the computed pressure and vorticity fields is shown. A quantitative comparison is made of the unsteady force on the channel walls. We demonstrate the numerical use of a volume-integral formula for computing the unsteady force. In the case of the finite difference method, more accurate results were obtained from this formula than by simply integrating the surface pressure on the channel walls due to the reduced accuracy of the solution near the boundaries. We also describe a direct way of computing pressure with the discrete vortex method.

Introduction

THE determination of the unsteady forces on the fluid boundaries is often the primary objective of a direct numerical simulation of an unsteady flow. The particular problem that motivates the work described here is the unsteady loading produced by the interaction of a cascade of airfoils with a nonuniform, incompressible inflow. This problem is relevant to turbomachines, such as pumps and marine propulsors, where the working fluid is nearly incompressible, and has been the subject of much study. Schorr and Reddy,[1] for example, derived an analytical solution for the interaction of a two-dimensional cascade of flat plates with a sinusoidal gust. More recently, Howe[2] analyzed the incompressible interaction of a helical line vortex with a two-dimensional cascade of flat plates. Only in studies of the interaction of an isolated airfoil with nonuniform flow have analysts relaxed the flat-plate assumption to include the effects of finite thickness[3-5] and mean loading and camber.[6] The importance of these effects on the unsteady loading of a cascade with nonuniform inflow is an open question. It may be possible to address this question with an analytical model, but only after making many simplifying assumptions. These assumptions can be avoided by performing a direct numerical simulation of the unsteady flow. Thus, the ultimate objective of our research is to use direct, three-dimensional numerical simulations to determine the effects of design parameters such as finite blade thickness on the unsteady loading of cascades.

Recently, Athavale and Merkle[7] and Rogers and Kwak[8] have conducted finite difference simulations of two-dimensional, unsteady, incompressible flows based on the time-accurate method of artificial compressibility. The former investigators neglected viscous terms, whereas the latter included them. A key feature of both implementations is the upwind-biased differencing of the convective terms in the equations of motion, which eliminates the need for artificial dissipation terms. One inherent attraction of this method is that it can be extended readily to three dimensions and, therefore, to unsteady three-dimensional flow in a cascade. The method has already been applied to steady-state flows in three dimensions by Hartwich and Hsu,[9] Kwak et al.,[10] and Tsai et al.[11]

In this paper, we test the time-accurate method of artificial compressibility, as implemented by Athavale and Merkle[7] and the present authors, on the model problem, shown in Fig. 1, of a compact vortex being convected by an inviscid mean flow through a converging/diverging channel. The solution is validated by comparison with the results of an entirely different numerical method, and the unsteady drag on the constricted region of the channel is computed from two different formulas. This test can be regarded as a step toward applying the time-accurate method of artificial compressibility to more complicated flows and, in particular, toward determining the effect of finite blade thickness on the unsteady loading of a cascade. Note that the geometry of the model problem can be transformed into a cascade of finite thickness airfoils by enforcing a periodicity condition in the cross-channel direction upstream and downstream of the constriction rather than a rigid-wall boundary condition. Such a cascade would experience unsteady lift and drag due to the change in the angle of attack as the vortex convects downstream, and it would be difficult to identify the unsteady drag component due to finite thickness. The model problem, on the other hand, effectively isolates the drag due to finite thickness, which is usually small in comparison to unsteady lift, but can be the dominant component of the unsteady load in some circumstances.[5] Thus, computing the unsteady drag in the model problem has some physical significance and represents a stringent test of a numerical method.

A key concern in applying the time-accurate method of artificial compressibility to the model problem was whether numerical dissipation in the upwind-biased spatial differencing scheme would cause the compact vortex to diffuse. We

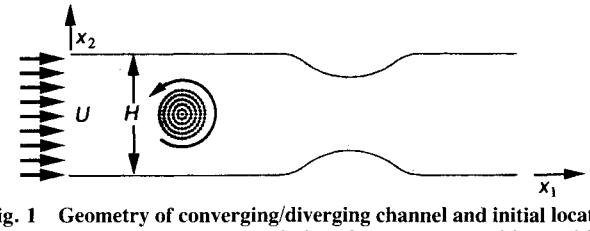

Fig. 1 Geometry of converging/diverging channel and initial location of compact vortex: concentric circles of dots are the initial positions of the vortex blobs used in the DVM simulation.

Received Aug. 24, 1990; revision received Jan. 9, 1991; accepted for publication Feb. 1, 1991.

*Senior Scientist, 70 Fawcett Street.
†Scientist, 70 Fawcett Street.
‡Engineer; currently, Senior Project Engineer, Saginaw Division, General Motors Corp., 3900 Holland Road, Saginaw, MI 48601.
§Engineer, 70 Fawcett Street. Member AIAA.

chose to represent the inflow disturbance in the model problem by a compact vortex rather than a sinusoidal gust, so that diffusion of the vorticity field would be readily apparent in contour plots, and to facilitate efficient solution of the same problem by the discrete vortex method (DVM). (The time-accurate method of artificial compressibility will, henceforth, be abbreviated by FDM, for finite difference method.) The DVM, being a grid-free method, has negligible numerical dissipation.[12] Therefore, diffusion of the compact vortex by the FDM, if present, would be readily apparent in the comparison of the FDM and DVM solutions. Viscous effects were neglected in both numerical methods since we are concerned with flows at high Reynolds number and inflow disturbances of large length scale relative to the thickness of the boundary layer on each airfoil of a cascade.

Good qualitative agreement between the FDM and DVM solutions is shown by comparing contour plots of the pressure and vorticity fields. The comparison shows that numerical diffusion of the vorticity is insignificant in the FDM as presently implemented, even with the fairly coarse grid used in the model problem. As an aside, we note that a novel method was used to compute the pressure field from the discrete vortex simulation. We solved a boundary-integral equation for the total pressure in the fluid and then obtained the static pressure from the algebraic relation between total pressure, static pressure, and velocity. This approach is direct and requires only a small additional computational effort over computing the velocity field alone.

The accuracy of the numerical solutions was also assessed quantitatively by comparing the unsteady force on the channel boundaries. This was computed by integrating the pressure on the boundaries and with an alternative formula derived by Howe,[5] which involves an integral over the fluid volume. Howe[5] contrasts this formula with alternative volume-integral formulations of the boundary force and notes its advantages. Computing the unsteady force from two different formulas provides a convenient self-validation of a numerical solution. For example, the surface and volume integrals produced nearly identical results in the case of the DVM, leading us to regard the DVM solution of the model problem as a benchmark. For the FDM, there were large discrepancies between the unsteady drag force computed from the surface and volume integrals although the latter agreed quite well with the DVM results. Based on the magnitude of the unsteady drag, we infer that the computed pressure field in the model problem must be accurate to within a few hundredths of a percent to reliably compute the unsteady drag due to finite thickness from a boundary integral.

In general, the results for the model problem give insight and instill confidence about applying the time-accurate method of artificial compressibility to more complicated problems. The comparison with the DVM shows that numerical diffusion of vorticity by the FDM is minor and should not be of concern. This is important when computing unsteady forces; they are directly related to the vorticity field, as Howe's formula shows, and would, therefore, be in error if the vorticity field suffers from numerical diffusion. From the comparison of unsteady drag force computed from two different formulas, we conclude that Howe's formula provides a more robust way of computing unsteady forces. Finally, the model problem demonstrates the high accuracy needed to reliably capture the effect of finite blade thickness on the unsteady loading of a cascade. We believe this is also an indication of the accuracy that will be needed in direct simulations of pumps and marine propulsors, where the unsteady thrust on a blade row is typically very small compared to the mean thrust.

Problem Formulation

We introduce a Cartesian coordinate system $\boldsymbol{x} = (x_1,x_2,x_3)$ and consider incompressible, inviscid flow in the domain D, which has an arbitrary stationary boundary ∂D. We denote the fluid velocity by $\boldsymbol{v}(\boldsymbol{x},t) = (v_1,v_2,v_3)$, where t is time, and the pressure by $p(\boldsymbol{x},t)$. The pressure and velocity must satisfy the continuity equation,

$$\nabla \cdot \boldsymbol{v} = 0 \tag{1}$$

and the momentum equation,

$$\frac{\partial \boldsymbol{v}}{\partial t} + \boldsymbol{v} \cdot \nabla \boldsymbol{v} = -\frac{\nabla p}{\rho} \tag{2}$$

where ρ is the constant fluid density.

Method of Artificial Compressibility

The method of artificial compressibility was originally suggested by Chorin[13] as a way of solving steady-state incompressible flow problems. The essence of the method for time-accurate problems is to modify the continuity equation (1) as follows:

$$\frac{\partial p}{\partial \tau} = -\beta \nabla \cdot \boldsymbol{v} \tag{3}$$

where β is an artificial compressibility parameter and the derivative of p with respect to the pseudotime τ is added to the continuity equation so that the pressure and velocity fields can be determined in a similar manner.

We have used the method as implemented by Athavale and Merkle.[7] In addition, we have independently implemented the method following the approach of Rogers and Kwak,[8] except that we omitted the viscous flux terms. Both approaches use third-order-accurate, upwind-biased, spatial differences and second-order-accurate time differences. The principal difference between the implementations is in the method used to solve the linear system that arises at each pseudotime step; Athavale and Merkle used approximate factorization, whereas we followed Rogers and Kwak and used a line relaxation scheme. We found that the pseudotime iterations converged more rapidly with the approximate factorization scheme.

Discrete Vortex Method

The DVM provides a grid-free approach to solving the equations of incompressible flow. A comprehensive review of the literature on all types of vortex methods is given by Sarpkaya.[14] Leonard[15] reviews the foundations of these methods in more detail. Our approach and notation are reminiscent of the work of Ghoniem and Gagnon[12] and Lee and Smith.[16] The rudiments of the method are reviewed here only as a precursor to show how pressure was evaluated in the field and on the boundary, an approach that we believe to be novel.

Any velocity field may be decomposed into an irrotational component $\boldsymbol{v}_\phi$ and a solenoidal component $\boldsymbol{v}_\omega$ such that

$$\boldsymbol{v} = \boldsymbol{v}_\phi + \boldsymbol{v}_\omega \tag{4}$$

Then, $\boldsymbol{v}_\phi$ can be obtained from the gradient of a scalar velocity potential ϕ as

$$\boldsymbol{v}_\phi = \nabla \phi \tag{5}$$

where ϕ satisfies the Laplace equation in D and the Neumann boundary condition

$$\boldsymbol{n} \cdot \nabla \phi = -\boldsymbol{n} \cdot \boldsymbol{v}_\omega \qquad \text{on} \qquad \partial D \tag{6}$$

where $\boldsymbol{n}$ is the unit normal to ∂D and is directed out of the fluid domain. We postpone momentarily the discussion of the way in which we numerically solved for ϕ.

The solenoidal velocity component can be related to the fluid vorticity, $\omega = \nabla \times v$, by

$$v_\omega(x,t) = \int_D K(x - y)\omega(y,t)\, d\tau(y) \tag{7}$$

where

$$\int_D d\tau(y)$$

denotes integration over D, and in two dimensions, with $r^2 = x_1^2 + x_2^2$,

$$K(x) = (-x_2,x_1)/2\pi r^2 \tag{8}$$

The DVM approximates the vorticity field as the sum of a finite number of discrete vortex blobs in the form

$$\omega(x,t) = \sum_n \Gamma_n f_\delta(x - x_n) \tag{9}$$

where Γ_n and x_n are the circulation and centroid, respectively, of the nth blob, and f_δ is the core function. The present results are for the second-order core function (cf. Ref. 17):

$$f_\delta(r) = e^{-r^2/\delta^2}/\pi\delta^2 \tag{10}$$

where δ is the nominal radius of the core. Upon substituting Eqs. (9) and (10) into Eq. (7), it can be shown that

$$v_\omega(x,t) = \sum_n \Gamma_n K(x - x_n)(1 - e^{-|x-x_n|^2/\delta^2}) \tag{11}$$

which is a discrete form of the Biot-Savart law in two dimensions.

At each time step, the two components of the velocity field must be computed at the blob centers x_n and the blob positions are updated by integrating

$$\frac{dx_n}{dt} = v(x_n,t) \tag{12}$$

We used a second-order-accurate predictor-corrector method to integrate Eq. (12).

We now return to consider the irrotational component v_ϕ. The discussion that follows is specialized for two dimensions, but the approach is completely general and can be applied in two or three dimensions. Define a Green function $G(x,y) = -\log r$, where $r = |x - y|$. Then Green's theorem may be applied to ϕ and G to obtain an integral equation for ϕ in the form

$$\alpha(x)\phi(x) - \oint_{\partial D} \phi(y) \frac{\partial G(x,y)}{\partial n_y}\, d\sigma(y) = \oint_{\partial D} \frac{\partial \phi(y)}{\partial n_y} G(x,y)\, d\sigma(y) \tag{13}$$

where

$$\oint_{\partial D} d\sigma(y)$$

denotes integration over ∂D, $\partial/\partial n_y = n(y) \cdot \nabla_y$, and

$$\begin{aligned} \alpha(x) &= 2\pi, && x \in D \\ &= \pi, && x \in \partial D \\ &= 0, && x \notin D \end{aligned} \tag{14}$$

We solved Eq. (13) by the usual method of discretizing ∂D into panels and assuming ϕ to be constant on each panel. We then computed v_ϕ on ∂D from central differences of ϕ. At interior points of D, we analytically differentiated Eq. (13) to compute v_ϕ.

The pressure distribution is needed in the fluid domain for the comparison with the method of artificial compressibility and on the boundaries to compute the net unsteady force. Sarpkaya[14] cites the absence of pressure in the formulation as one of the drawbacks of the DVM because it inhibits the direct comparison of numerical results with experimental data (or with primitive variable solutions, as in the present work). Previous investigators (cf. Ref. 16) have computed pressure by the indirect approach of integrating the momentum equation along a streamline. This integration is performed most easily on a solid boundary, which must coincide with a streamline. However, obtaining the pressure at specified internal points of the fluid domain is more difficult since the streamline passing through a particular point is a priori unknown. Here we introduce a direct way of evaluating the pressure distribution that requires only a minor additional computational effort at each time step and avoids the difficulty and inaccuracy of integrating along a streamline.

Define the total pressure referenced to the freestream total pressure as

$$B \equiv p - p_\infty + \tfrac{1}{2}\rho(v^2 - U^2) \tag{15}$$

where p_∞ is the reference pressure, U is the uniform freestream velocity, and $v = |v|$. Then it is shown in the Appendix that B satisfies the Poisson equation,

$$\nabla^2 B = -\rho \nabla \cdot (\omega \times v) \tag{16}$$

which can be shown to be equivalent to the well-known Poisson equation for pressure,

$$\nabla^2 p = 2\rho\left(\frac{\partial v_1}{\partial x_1}\frac{\partial v_2}{\partial x_2} - \frac{\partial v_1}{\partial x_2}\frac{\partial v_2}{\partial x_1}\right) \tag{17}$$

Since ω appears explicitly in the inhomogeneous term, Eq. (16) relates B to the rotational component of the flow. This contrasts with Eq. (17), where the inhomogeneous term is nontrivial even if the flow is irrotational. We show in the Appendix that B can be obtained by solving the integral equation,

$$\alpha(x)B(x) - \oint_{\partial D} B(y) \frac{\partial G(x,y)}{\partial n_y}\, d\sigma(y) = -\rho \int_D \nabla_y G \cdot (\omega \times v)\, d\tau(y) \tag{18}$$

where $\alpha(x)$ is defined in Eqs. (14). Note that the operator on B on the left side of Eq. (18) is identical to the operator on ϕ on the left side of Eq. (13); thus, no additional computational effort is required to set up and factor the matrix associated with the discretized form of Eq. (18). The integral on the right side of Eq. (18) is computed easily by a discrete approximation of the form

$$-\int_D \nabla_y G \cdot (\omega \times v)\, d\tau(y) \cong -\sum_n \Gamma_n \left[\frac{\partial G(x,y_n)}{\partial y_2} v_1(y_n) - \frac{\partial G(x,y_n)}{\partial y_1} v_2(y_n)\right] \tag{19}$$

Once B has been computed at a point either within the fluid or on the boundary, the pressure can be evaluated from Eq. (15), where v^2 is determined just as it is at the centroid of a

vortex blob. The accuracy of the pressure field computed by this approach is the same as the accuracy of the irrotational component of the velocity field.

Formulas for Boundary Forces

The obvious way to compute the unsteady force on ∂D is to integrate the wall pressure. Denoting the ith component of the unsteady force by $F_i(t)$, we have

$$F_i(t) = \oint_{\partial D} p(\boldsymbol{x},t) n_i(\boldsymbol{x})\, d\sigma(\boldsymbol{x}) \tag{20}$$

where n_i is the ith component of the unit normal to ∂D.

Howe[5] has derived an alternative formula for the unsteady force on an arbitrary rigid body translating in an incompressible, viscous fluid. We define the normalized velocity potential

$$X_i(\boldsymbol{x}) = x_i + \varphi_i(\boldsymbol{x}) \tag{21}$$

where the first term represents a uniform flow of unit speed in the ith direction, and $\varphi_i(\boldsymbol{x})$ is the corresponding perturbation potential due to the presence of the body. Then, for the special case of a stationary boundary and an inviscid fluid, Howe's formula reduces to

$$F_i = \rho \int_D \nabla X_i \cdot (\omega \times \boldsymbol{v})\, d\tau \tag{22}$$

where the dependence of all quantities except X_i on t is implicit. The domain of integration in this case is over the entire fluid volume D. It is often the case, however, that the vorticity is nonzero only in a compact region of the fluid domain and the range of integration in Eq.(22) may be restricted to that region.

In a simulation based on the method of artificial compressibility, the unsteady force can be evaluated at the beginning or end of each pseudotime iteration. Computing the force from the surface integral, Eq. (20), is straightforward; we tried the trapezoidal rule and Simpson's rule and found negligible differences in the unsteady force. Implementing the volume integral formulation is more difficult since the vorticity and the normalized velocity potential X_i are not directly available from the finite difference formulation. We obtained the vorticity from cell-centered differences of the velocity field. A range of techniques are available for solving the Laplace equation for X_i. We used the boundary-integral equation (13) with ϕ replaced by φ_i and $\partial\varphi_i/\partial n_y = -n_i$ to solve for X_i on the boundaries. Note, however, that Eq. (22) calls for the gradient of X_i. We obtained the gradient at internal grid points by analytically differentiating the boundary-integral formulation and at points on the boundaries by second-order finite differences. Regardless of the method used to obtain ∇X_i, this computation can be performed once and for all at the start of the simulation.

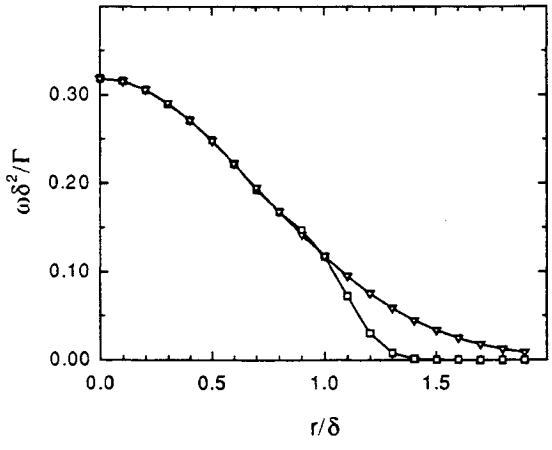

Fig. 2 Comparison of the analytic form of the initial vorticity distribution (—▽—) and the approximate distribution obtained with N = 131 vortex blobs in the positions shown in Fig. 1 (—□—).

With the discrete vortex method as outlined earlier, all quantities needed to evaluate the unsteady force on the boundary from Eq. (22) are readily available. We assumed that ν is constant within the core of each blob and approximated Eq. (22) by

$$F_i = \rho \sum_n \Gamma_n \left[\frac{\partial X_i}{\partial x_2} v_1 - \frac{\partial X_i}{\partial x_1} v_2 \right] \tag{23}$$

where the quantity inside the square brackets is evaluated at $\boldsymbol{x} = \boldsymbol{x}_n$. The unsteady force was also evaluated from Eq. (20) using the pressure distribution determined by solving Eq. (18).

Convection of Compact Vortex Through a Converging/Diverging Channel

We have used both the FDM and DVM to simulate convection of a compact vortex by the inviscid mean flow through the converging/diverging channel shown in Fig. 1. Henceforth, all quantities are normalized on ρ, U, and $2H$, where U is the uniform mean flow velocity far upstream of the constriction and H is the channel height. The thickness of the bumps on the channel walls is $0.2H$; they were constructed from circular arcs of radius $0.725H$ with circular arc fillets of radius $0.4H$ at the upstream and downstream junctions with the channel walls. We specified an initial vorticity distribution of the form

$$\omega(\boldsymbol{x},t=0) = \frac{\Gamma_T e^{-r^2/\delta_T^2}}{\pi\delta_T^2}, \qquad r = |\boldsymbol{x} - \boldsymbol{x}_0| \tag{24}$$

where Γ_T is the total circulation, δ_T the core radius, and $\boldsymbol{x}_0 = (x_0,y_0)$ the initial position of the vortex center.

The initial conditions are a critical issue in an unsteady flow simulation. One approach is to start with nonphysical initial conditions, impose unsteady boundary conditions, and run the simulation until the startup transients decay. For example, Athavale and Merkle[7] specified a sinusoidal perturbation of the inflow velocity. To solve the present model problem, however, the FDM simulation has to be started with initial pressure and velocity distributions that are completely consistent with the governing equations. We approximated the initial vorticity distribution, Eq. (24), by N vortex blobs of the form of Eq. (10). Then we obtained the solenoidal component of the velocity field from Eq. (11) and solved Eq. (13) for the irrotational component. We used Eqs. (18) and (15) to obtain the initial pressure distribution. These equations must be solved at each time step of the DVM in any case, so no extra effort was required. The velocity and pressure fields so obtained were then used to initiate the FDM simulations.

For the case $\Gamma_T/2UH = 0.2$, $\delta_T/2H = 0.1$, and $(x_0,y_0)/H = (1.0,0.5)$, the initial vorticity distribution was approximated by five rings of vortex blobs totaling $N = 131$ blobs in all and with $\delta_n/2H = 0.02$ for all blobs. The initial positions of the blob centers are indicated by the concentric circles of dots in Fig. 1. Figure 2 compares the analytical vorticity distribution given by Eq. (24) and the approximate distribution as computed from Eq. (9). The approximation in the region $r/\delta > 1$ could have been improved by adding more rings of blobs. The total circulation provided by the approximate distribution was $\Gamma_A/2UH = 0.15$, where

$$\Gamma_A = \sum_{n=1}^{N} \Gamma_n \tag{25}$$

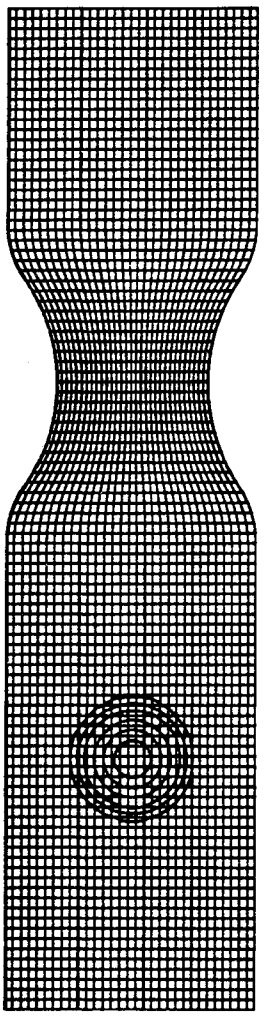

Fig. 3 100 × 32 grid for FDM simulation and contours of initial vorticity distribution.

The finite difference grid is shown in Fig. 3 with the initial vorticity contours superposed on it. The grid consisted of 100 points in the x_1 direction and 32 points in the x_2 direction. The initial velocity and pressure distributions were obtained from the first time step of the DVM simulation as described earlier. The simulations reported herein were based on the values of $\beta = 1.0$ and $\Delta\tau U/2H = 10^5$.

In both the DVM and FDM simulations, we specified a uniform velocity profile at the inflow boundary and static pressure $p = 0$ at the outflow boundary. In the DVM simulations, we also imposed a uniform velocity profile at the outflow boundary.

Numerical Results

Here we compare the time evolution of the pressure and velocity field predicted by the two methods. The comparison focuses on the case $\Gamma_T/2UH = 0.2$, $\delta_T/2H = 0.1$ with initial position $(x_0,y_0)/H = (1.0,0.5)$; however, we briefly consider the effects of varying the vortex strength and number of blobs. To give the vortex circulation some physical significance, we note that the maximum perturbation velocity induced by a vortex of strength $\Gamma_T/2UH = 0.2$ occurs at the edge of the core and is of magnitude $0.2U$. This is larger than the maximum turbulence intensity in the inflow to a typical pump or marine propulsor; thus, a vortex of circulation $\Gamma_T/2UH = 0.2$ can be regarded as a fairly strong vortex.

Figure 4 shows the contours of pressure and vorticity at the times $tU/2H = 0.5$, 0.7, and 0.9. The upper and lower plots at each time show results from the DVM and FDM, respectively. Unless otherwise stated, the FDM results were obtained with the code developed for Ref. 7. There is very good qualitative agreement between the DVM and FDM results. The distortion of the vortex as it convects through the constricted section is readily apparent from the vorticity contours. Downstream of the constriction, the vorticity contours return to their original circular shape, showing that the momentum loss due to numerical diffusion is small. However, in the FDM results, we notice that vorticity is present near the channel walls in the vicinity of the constriction and downstream of it. This spurious vorticity is an indication of excessive error in the solution in these regions.

Although the visual agreement of the DVM and FDM results in Fig. 4 is gratifying, a quantitative measure of their accuracy can be made by comparing the time histories of net streamwise force on the channel walls. Figure 5 shows the net streamwise force as computed using Eqs. (20) and (22) (the surface- and volume-integral formulas, respectively) for both the DVM and FDM simulations. For the DVM, the agreement between the two formulas is within the resolution of the graph. For the FDM, the net force computed from Eq. (22) is in fair agreement with the DVM results; however, large discrepancies are evident in the force computed from Eq. (20). We attribute these differences to the spurious vorticity observed near the walls in Fig. 4.

Comparing the net force to the freestream dynamic pressure gives a measure of how accurate the pressure distribution on the channel walls must be to accurately compute the net force from Eq. (20). We define an average unsteady pressure p' by dividing the net force by the channel height, i.e., $p' = F_1/H$. Normalizing p' by the freestream dynamic pressure gives $p'/\frac{1}{2}\rho U^2 = F_1/\frac{1}{2}\rho U^2 H$; therefore, we see from Fig. 5 that p' is on the order of 1.0% of the freestream dynamic pressure. This implies, for the present case, that the pressure distribution on the channel walls must be accurate to at least three significant figures to compute the unsteady force to one or two significant places.

Despite the fact that a vortex of circulation $\Gamma_T/2UH = 0.2$ is fairly strong from a practical perspective, it is barely distinguishable in the contour plots of static pressure in Fig. 4. We found, on the other hand, that contours of total pressure clearly show the presence of the vortex and convey much the same information as contours of vorticity. The initial distributions of $(p - p_\infty)/\rho U^2$, $\frac{1}{2}(1 - v^2/U^2)$, and $B/\rho U^2$, as computed with the DVM, are shown in Fig. 6. For purposes of comparison, the same contour levels are shown for all three quantities. The vortex is barely visible upstream of the constriction in the contour plot of $(p - p_\infty)/\rho U^2$, whereas the pressure gradients associated with the mean flow are clearly visible in the vicinity of the constriction. The contour plot of $\frac{1}{2}(1 - v^2/U^2)$, which is the dynamic pressure in the case of a steady irrotational flow, shows the presence of the vortex more clearly, but is nearly the same as the pressure contours in the region of the constriction where there is no vorticity. The gradients associated with the vortex also appear clearly in the contour plot of $B/\rho U^2$, but the mean-flow gradients are absent. Thus, the contour plot of $B/\rho U^2$ highlights vorticity in the flow by filtering out gradients associated with the underlying irrotational flow.

This effect is further demonstrated in Fig. 7, which shows contour plots of the same three quantities at $tU/2H = 0.7$, when the vortex is near the narrowest part of the channel. Again, the contours of $(p - p_\infty)/\rho U^2$ primarily show the underlying mean flow, whereas the steady and unsteady components are inseparable in the contour plot of $\frac{1}{2}(1 - v^2/U^2)$. The contour plot of $B/\rho U^2$, however, shows the same characteristic pattern of a vortex as Fig. 6, albeit somewhat distorted by the presence of the constriction. Thus, even when the vortex is in the region where the irrotational flow gradients are strongest, visualizing $B/\rho U^2$ provides a way of distinguishing the irrotational and solenoidal flow components. Of course, the same information can be obtained by plotting contours of

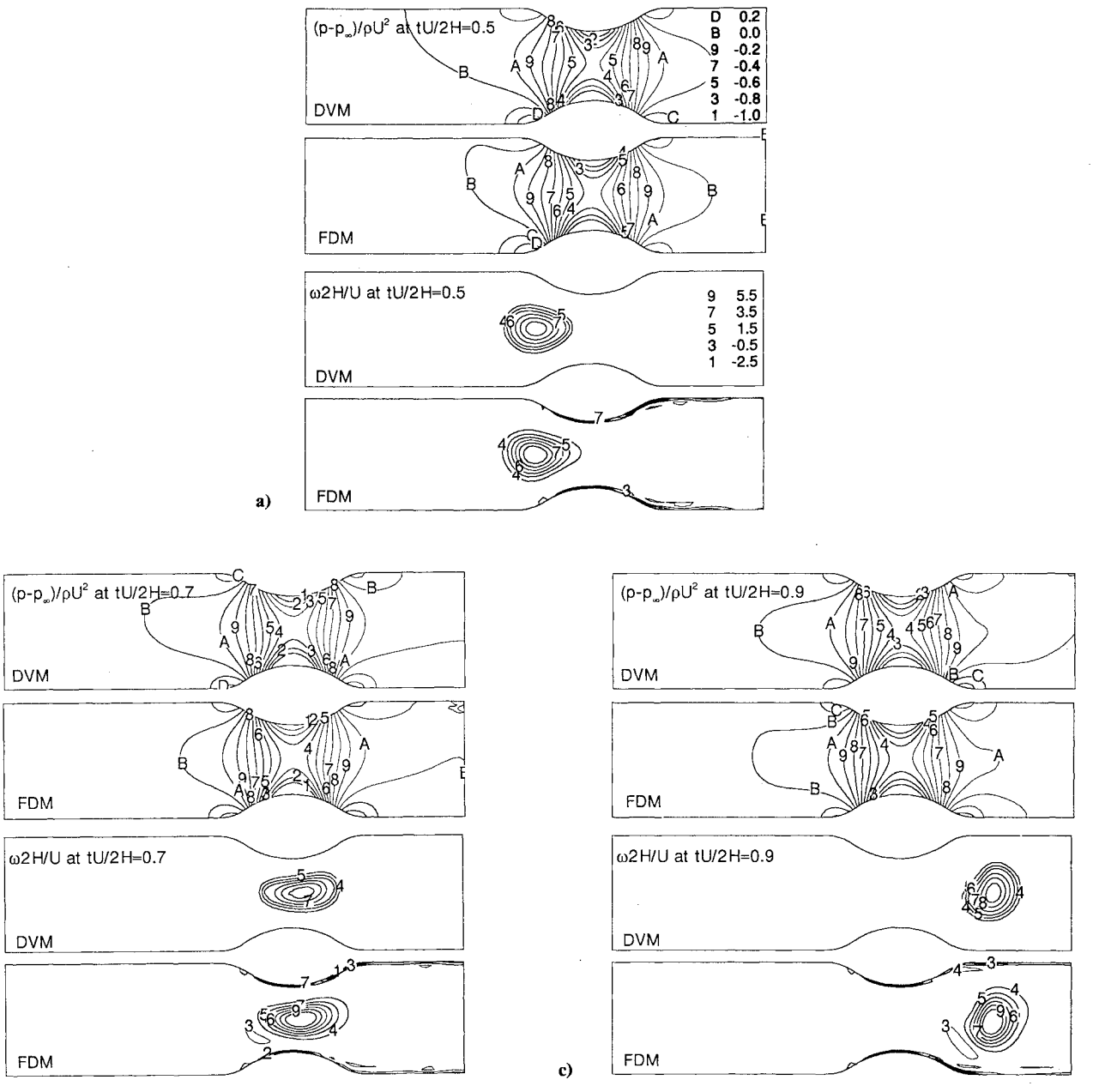

Fig. 4 Contours of pressure and vorticity at three times for $\Gamma_T/2UH = 0.2$, $\delta_T/2H = 0.1$, and $(x_0,y_0)/H = (1.0,0.5)$. The upper and lower plots at each time show results from the DVM and FDM, respectively. All pressure plots have the same contour levels and all vorticity plots have the same contour levels.

vorticity, but there are several advantages to plotting total pressure. Total pressure can be obtained directly from experimental measurements if both pressure and velocity are measured, whereas vorticity can only be measured by indirect means.[18–20] Furthermore, in three dimensions, we anticipate that it will be easier to visualize the total pressure scalar than the vorticity vector.

We used contour plots of total pressure to investigate the accuracy of the FDM solution in the vicinity of the channel walls. Figure 8 shows contours of $B/\rho U^2$ at $tU/2H = 0.7$ based on the DVM and two independent FDM solutions. The DVM results are repeated from Fig. 7 for purposes of comparison. The three plots are qualitatively similar, however, the FDM results show irregularities upstream of the constriction and near the walls downstream of it. The level of the irregular contour upstream of the constriction is close to zero, and so its shape is quite sensitive to the particular choice of contour levels; a different choice of levels would have obscured the differences among the plots, at least upstream of the con-

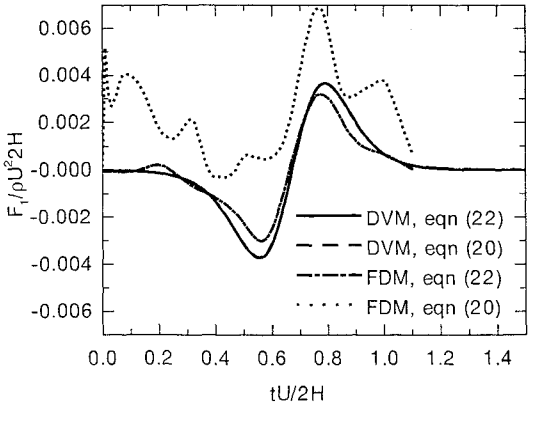

Fig. 5 Net streamwise force on channel walls for $\Gamma_T/2UH = 0.2$, $\delta_T/2H = 0.1$, and $(x_0,y_0)/H = (1.0,0.5)$ as computed using Eqs. (20) and (22) for both the DVM and FDM simulations.

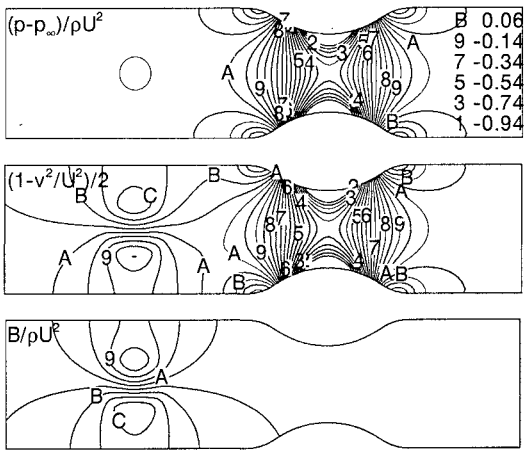

Fig. 6 Contours of $(p - p_\infty)/\rho U^2$, $\frac{1}{2}(1 - v^2/U^2)$, and $B/\rho U^2$ at $tU/2H = 0.0$ for $\Gamma_T/2UH = 0.2$, $\delta_T/2H = 0.1$, and $(x_0,y_0)/H = (1.0,0.5)$: contour levels are the same for all quantities.

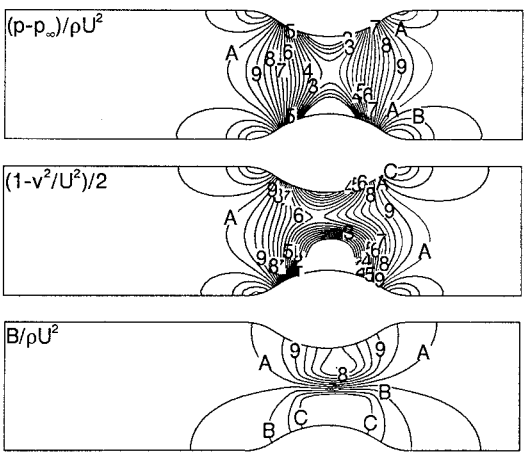

Fig. 7 Same contours as Fig. 6, except at $tU/2H = 0.7$.

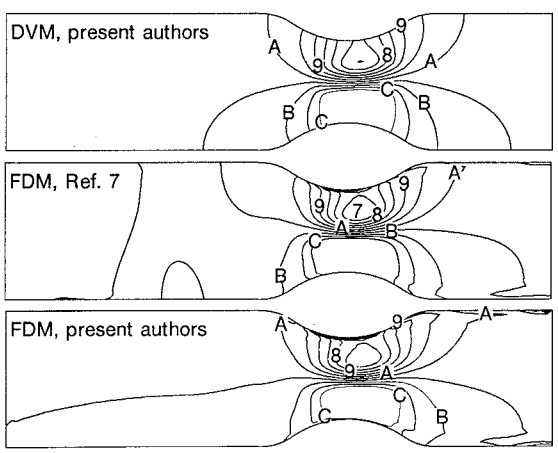

Fig. 8 Contours of $B/\rho U^2$ at $tU/2H = 0.7$ for $\Gamma_T/2UH = 0.2$, $\delta_T/2H = 0.1$, and $(x_0,y_0)/H = (1.0,0.5)$ based on the DVM and two FDM implementations: contour levels are the same as in Figs. 6 and 7.

striction. The irregularities near the walls downstream of the constriction, particularly near the lower wall, are more pervasive in that they affect all contour levels. Given the direct relationship between B and vorticity, these irregularities are another confirmation of the spurious vorticity generated on the constricted part of the channel walls in the FDM simulations. Since our implementation of the FDM was completely independent of the Athavale and Merkle implementation and

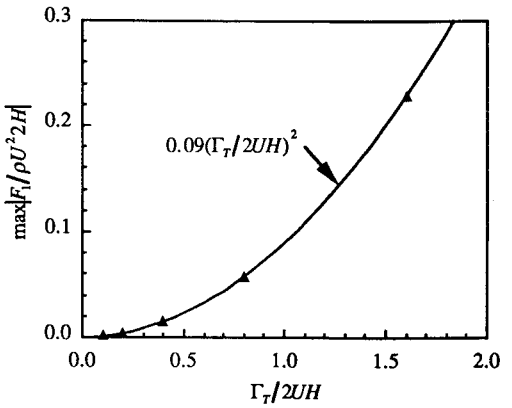

Fig. 9 Maximum absolute value of net streamwise force based on DVM (▲) and curve fit (——).

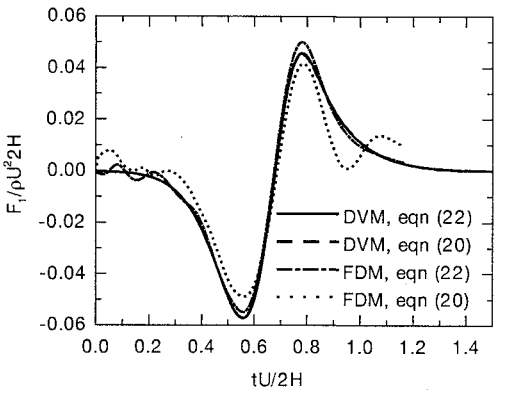

Fig. 10 Same as Fig. 5, except for $\Gamma_T/2UH = 0.8$.

both implementations generated the spurious vorticity, we believe that there is a fundamental problem with the boundary conditions in the FDM implementations rather than a programming error in either implementation.

The present model problem is a stringent test of a numerical method because the net streamwise force varies quadratically with the vortex circulation, as demonstrated in Fig. 9. By comparison, consider the much studied airfoil-vortex interaction problem where the unsteady lift force is linear and the unsteady drag force is quadratic in the vortex circulation.[5] The unsteady drag is much smaller than the unsteady lift on the airfoil. Since the net streamwise force in the present model problem is, roughly speaking, equivalent to the unsteady drag in the airfoil-vortex interaction problem, it is in some sense a small quantity, which is difficult to compute with accuracy.

In view of the quadratic dependence of the streamwise force on circulation, we expected the accuracy of the FDM to improve considerably if we increased the circulation. This was indeed the case, as shown in Fig. 10, where we have plotted the same quantities as in Fig. 5, but for a vortex with four times as much circulation, i.e., $\Gamma_T/2UH = 0.8$. There is a marked improvement in the agreement between the FDM results based on Eqs. (20) and (22), although there is still a large anomaly in the force computed from Eq. (20) after the vortex passes through the narrowest channel section. Presumably the agreement would be even better if the vortex circulation were increased still further. This trend supports our comment that the volume integral formula, Eq. (22), is more robust than Eq. (20) when the accuracy of the solution is suspect near the solid boundaries.

Concluding Remarks

We have used the DVM and the FDM to simulate an unsteady, inviscid, incompressible flow problem. From the good qualitative agreement between the methods, we conclude that

both methods provide correct solutions of the governing equations, at least in the internal portion of the fluid domain.

The initial pressure and velocity distributions were computed with the DVM and then used to initiate the FDM simulations. We observed that even if the initial pressure distribution was incompatible with the initial velocity distribution, the FDM quickly recovered the correct pressure distribution. Moreover, the evolution of the vorticity field was only weakly affected by the initial pressure distribution, and the time history of net streamwise force was not substantially affected. We regard this insensitivity to the initial pressure distribution as a symptom of the weak coupling between pressure and velocity in the governing equations. It is reassuring to see that the method of artificial compressibility overcomes the weak coupling to recover the correct pressure.

Comparing the unsteady force as computed from the surface integral, Eq. (20), and Howe's formula, Eq. (22), is a useful way of checking numerical solutions. Based on this comparison, we judged the DVM to be more accurate than the FDM for the case studied. Since the error in the force computed with the FDM and Eq. (20) decreased when the vortex circulation was increased, whereas the error in the force computed with the FDM and Eq. (22) was independent of the vortex circulation, we suggest that Howe's formula provides a more robust way of computing the unsteady force.

We can only speculate about the source of the spurious vorticity observed near the channel walls in the FDM solution. Perhaps this vorticity is a consequence of the reduced order of the spatial differences at the walls; the spatial differences at internal grid points were third-order accurate, whereas the boundary conditions were second-order accurate. Since the vorticity field must be obtained by differencing the velocity field, it is second-order accurate at internal grid points and only first-order accurate at the boundaries. Reducing the grid spacing in the region adjacent to the wall would improve the accuracy of the solution there. This would be necessary, in any case, if we were solving the Reynolds-averaged or thin-layer Navier-Stokes equations instead of the Euler equations.

We believe that the study of a model problem such as the one investigated here is a useful way of checking unsteady, inviscid, incompressible flow simulations. The simulation can be qualitatively judged by examining contour plots of the vorticity field, and its accuracy can be quantitatively assessed by comparing the net streamwise force based on the surface integral and Howe's formula.

Appendix: Derivation of Equation (18)

Here we derive the integral equation (18) that relates the total pressure B to the velocity and vorticity fields. We start with the equations governing incompressible, inviscid flow: the continuity equation,

$$\nabla \cdot v = 0 \tag{A1}$$

and Crocco's form of the momentum equation (cf. Ref. 21),

$$\frac{\partial v}{\partial t} + \frac{\nabla B}{\rho} = -(\omega \times v) \tag{A2}$$

Taking the divergence of Eq. (A2) and making use of Eq. (A1) gives a Poisson equation for B of the form

$$\nabla^2 B = -\rho \nabla \cdot (\omega \times v) \tag{A3}$$

which can be shown to be equivalent to the well-known Poisson equation for pressure. We will also need the Green function $G(x,y) = -\log r$, where $r = |x - y|$, which satisfies

$$\nabla^2 G = -2\pi\delta(x - y) \tag{A4}$$

where δ is the Dirac delta function.

Substituting B and G in Green's theorem gives

$$\int_D [B\nabla_y^2 G - G\nabla_y^2 B]\, d\tau(y) = \oint_{\partial D} \left[B \frac{\partial G}{\partial n_y} - G \frac{\partial B}{\partial n_y} \right] d\sigma(y) \tag{A5}$$

Next we use Eqs. (A3) and (A4) on the left side of Eq. (A5) and the vector identity

$$\nabla \cdot G(\omega \times v) = G\nabla \cdot (\omega \times v) + \nabla G \cdot (\omega \times v) \tag{A6}$$

to put Eq. (A5) in the form

$$2\pi B(x) + \oint_{\partial D} B(y) \frac{\partial G}{\partial n_y} d\sigma(y) = -\rho \int_D \nabla G \cdot (\omega \times v)\, d\tau(y) + \oint_{\partial D} G \frac{\partial B}{\partial n_y} d\sigma(y) + \rho \int_D \nabla \cdot G(\omega \times v)\, d\tau(y) \tag{A7}$$

Applying the divergence theorem to the last term gives

$$2\pi B(x) + \oint_{\partial D} B(y) \frac{\partial G}{\partial n_y} d\sigma(y) = -\rho \int_D \nabla G \cdot (\omega \times v)\, d\tau(y) + \oint_{\partial D} Gn \cdot [\nabla B + \rho(\omega \times v)]\, d\sigma(y) \tag{A8}$$

Finally, we use Eq. (A2) to replace the last term of Eq. (A8) by

$$\rho \oint_{\partial D} G \frac{\partial}{\partial t} (n \cdot v)\, d\sigma(y) \tag{A9}$$

which vanishes due to the Neumann boundary condition (6). Thus, B may be obtained at any interior point $x \in D$ from the integral equation

$$2\pi B(x) + \oint_{\partial D} B(y) \frac{\partial G}{\partial n_y} d\sigma(y) = -\rho \int_D \nabla G \cdot (\omega \times v)\, d\tau(y) \tag{A10}$$

Generalizing this equation for arbitrary x leads to Eq. (18).

Acknowledgments

This work has been supported by the Office of Naval Research Accelerated Research Initiative on Hydroacoustics of Unsteady Flows through Contract N00014-89-C-0254. Partial support of this research was also provided through a grant from the Pittsburgh Supercomputing Center. We thank Charles L. Merkle of Pennsylvania State University for providing the finite difference computer code described in Ref. 7.

References

[1]Schorr, B., and Reddy, K. C., "Inviscid Flow Through Cascades in Oscillatory and Distorted Flow," *AIAA Journal*, Vol. 9, No. 10, 1971, pp. 2043–2050.

[2]Howe, M. S., "Blade-Vortex Interaction Noise in Two-Dimensional Cascade Flow," Bolt, Beranek and Newman, Cambridge, MA, Rept. 7257, Jan. 1990; also, *Journal of Sound and Vibration* (to be published).

[3]Hawkings, D. L., "A Possible Unsteady Thickness Noise Mechanism for Helicopter Rotors," *Journal of the Aeronautical Society of America*, Vol. 63, Supp. 1, Spring 1978, pp. 521–522.

[4]Glegg, S. A. L., "Significance of Thickness Noise Sources," *AIAA Journal*, Vol. 25, No. 6, 1987, pp. 839–844.

[5]Howe, M. S., "On Unsteady Surface Forces and Sound Produced by the Normal Chopping of a Rectilinear Vortex," *Journal of Fluid Mechanics*, Vol. 206, Sept. 1989, pp. 131–153.

[6]Atassi, H. M., "The Sears Problem for a Lifting Airfoil Revisited—New Results," *Journal of Fluid Mechanics*, Vol. 141, April 1984, pp. 109–122.

[7]Athavale, M. M., and Merkle, C. L., "An Upwind Differencing Scheme for Time-Accurate Solutions of Unsteady Incompressible Flow," AIAA Paper 88-3650, July 1988.

[8]Rogers, S. E., and Kwak, D., "Upwind Differencing Scheme for the Time-Accurate Incompressible Navier-Stokes Equations," *AIAA Journal*, Vol. 28, No. 2, 1990, pp. 253–262.

[9]Hartwich, P. M., and Hsu, C. H., "High-Resolution Upwind Schemes for the Three-Dimensional Incompressible Navier-Stokes Equations," *AIAA Journal*, Vol. 26, No. 11, 1988, pp. 1321–1328.

[10]Kwak, D., Chang, J. L. C., Shanks, S. P., and Chakravarthy, S. R., "A Three-Dimensional Incompressible Navier-Stokes Flow Solver Using Primitive Variables," *AIAA Journal*, Vol. 24, No. 3, 1986, pp. 390–396.

[11]Tsai, P. Y. L., Merkle, C. L., and Huang, T. T., "Euler Equation Analysis of the Propeller-Wake Interaction," *Proceedings of the 7th Symposium on Naval Hydronamics*, National Academy Press, Washington, DC, 1989, pp. 431–444.

[12]Ghoniem, A. F., and Gagnon, Y., "Vortex Simulation of Laminar Recirculating Flow," *Journal of Computational Physics*, Vol. 68, No. 2, 1987, pp. 346–377.

[13]Chorin, A. J., "A Numerical Method for Solving Incompressible Viscous Flow Problems," *Journal of Computational Physics*, Vol. 2, No. 1, 1967, pp. 12–26.

[14]Sarpkaya, T., "Computational Methods with Vortices—The 1988 Freeman Scholar Lecture," *Journal of Fluids Engineering*, Vol. 111, No. 1, 1989, pp. 5–52.

[15]Leonard, A., "Vortex Methods for Flow Simulation," *Journal of Computational Physics*, Vol. 37, No. 3, 1980, pp. 289–335.

[16]Lee, D. J., and Smith, C. A., "Distortion of the Vortex Core During Blade/Vortex Interaction," AIAA Paper 87-1243, June 1987.

[17]Beale, J. T., and Majda, A., "High Order Accurate Vortex Methods with Explicit Velocity Kernels," *Journal of Computational Physics*, Vol. 58, No. 2, 1985, pp. 188–208.

[18]Agui, J. C., and Jimenez, J., "On the Performance of Particle Tracking," *Journal of Fluid Mechanics*, Vol. 185, Dec. 1987, pp. 447–468.

[19]Imaichi, K., and Ohmi, K., "Numerical Processing of Flow-Visualization Pictures: Measurement of Two-Dimensional Vortex Flow," *Journal of Fluid Mechanics*, Vol. 129, April 1983, pp. 283–311.

[20]Cantwell, B., and Coles, D., "An Experimental Study of Entrainment and Transport in the Turbulent Near Wake of a Circular Cylinder," *Journal of Fluid Mechanics*, Vol. 136, Nov. 1983, pp. 321–374.

[21]Liepmann, H. W., and Roshko, A., *Elements of Gasdynamics*, Wiley, New York, 1957, p. 193.